Enhancing performance of molybdenum doped strontium ferrite electrode by surface modification through Ni infiltration

Jiahui Xu,[a] Shuaibin Wan,[b] Yao Wang,[*a] Su Huang,[a] Zhihao Yuan,[c] Fanglin Chen,[d] Yanxiang Zhang[*b] and Tong Liu[*a]

[a] *Key Laboratory of Hydraulic Machinery Transients (Wuhan University), Ministry of Education, School of Power and Mechanical Engineering, Wuhan University, Wuhan, Hubei 430072, China*

[b] *National Key Laboratory for Precision Hot Processing of Metals, School of Materials Science and Engineering, Harbin Institute of Technology, Harbin, Heilongjiang 150001, China*

[c] *School of Materials Science and Engineering, Tianjin University of Technology, Tianjin 300384, China*

[d] *Department of Mechanical Engineering, University of South Carolina, Columbia, SC 29208, USA*

* Corresponding Information

Email: liu_tong@whu.edu.cn (T. L.), pmewy@whu.edu.cn (Y. W.), hitzhang@hit.edu.cn (Y. Z.)

Abstract

Molybdenum doped strontium ferrite, $Sr_2Fe_{1.5}O_{0.5}O_6$ (SFM), is a promising perovskite-type hydrogen electrode material in solid oxide cells (SOCs), but usually suffers from insufficient electro-catalytic activity. Herein, Ni nanoparticles with high electro-catalytic properties have been infiltrated into $Sr_2Fe_{1.5}O_{0.5}O_6$ (SFM) scaffold to form Ni-SFM electrode with high electro-catalytic activity for power generation and CO_2 electro-reduction. Pre-sintering temperature and Ni loading of Ni-SFM electrodes have been systematically investigated to minimize the electrode polarization resistance (R_p). R_ps of bare SFM electrode vary significantly with pre-sintering temperature, and the

lowest R_p value of 1.04Ωcm^2 is obtained for bare SFM electrode pre-fired at 1050°C. Moreover, a significantly reduced R_p value of 0.32Ωcm^2 is achieved at 800°C after Ni infiltration. Additionally, three-dimensional microstructure of Ni-SFM electrode is simulated numerically, and geometric properties including Ni/SFM/gas triple-phase-boundaries (TPBs) length, Ni/SFM interfacial area, and Ni surface area are calculated under various Ni loadings to correlate electrode microstructure with electrode performance, revealing that the electrode performance are strongly affected not only by the TPBs but also the interface area. Enhanced electrochemical performance indicate that Ni-SFM electrode is a promising high-performance hydrogen electrode for SOCs application.

Key words: Solid oxide cell; Infiltration; Nanostructured electrode; Molybdenum doped strontium ferrite; 3D numerical simulation

1. Introduction

Solid oxide cell (SOC), a promising energy conversion and storage device[1-7], is attracting much attention because of its advantages of high heat and power conversion efficiency, relatively low cost, modular operation, environmental benign, etc. One of the challenges for the practical application of SOC technologies is the lack of hydrogen electrode that can operate directly in both solid oxide fuel cell (SOFC) and solid oxide electrolysis cell (SOEC) modes with high efficiency and stability. The state-of-the-art Ni-based cermet hydrogen electrodes exhibit excellent electrochemical performance, but suffer from microstructure change and redox instability, resulting in electrochemical performance degradation due to the fuel supply interruption, gas sealing failure and redox cycling[8-13]. On the other hand, in recent years, perovskite type (ABO_3) oxide materials, such as $Sr_2Fe_{1.5}Mo_{0.5}O_6$ (SFM)[14-21], $La_{0.8}Sr_{0.2}Cr_{0.5}Mn_{0.5}O_{3-\delta}$ (LSCrMn)[22-24], and donor-doped $SrTiO_3$[25-27] have been intensively explored as alternative hydrogen electrodes because of their robust stability against redox cycling. However, these Ni-free ceramic hydrogen electrodes typically exhibit inadequate catalytic activity for hydrocarbon fuel oxidation or H_2O/CO_2 splitting reaction[28-30]. Therefore, perovskite oxide hydrogen electrodes usually need to be further improved to enhance the electrocatalytic activity. In this work, perovskite oxide SFM has been chosen as the scaffold material because of its high melting point, good electrochemical performance and excellent resistance against redox cycling[14], and infiltration of Ni to SFM has been performed to enhance its electrocatalytic activity.

Optimization of perovskite oxide hydrogen electrode microstructure for improved performance has been commonly applied in the development of SOCs. Recently, to effectively enhance electrode performance, nano-catalysts, which can be highly-performed metallic catalysts such as Ni, Co, Ag,

Cu, and Ru [31-37] or oxide catalysts such as cerium oxide (CeO_2) [38,39], Gd-doped CeO_2 [40,41], $PrBaMn_2O_{5+\delta}$ (PBM) [42,43], and $Sr_2Fe_{1.5}Mo_{0.5}O_{6-\delta}$ (SFM) [20,44] have been commonly introduced into the porous oxide electrodes to form a nanostructured electrode to drastically accelerate some aspect of the electrode processes. The nanoparticles are typically added through solution infiltration processes that involve the precipitation of a metal salt in the pores of the pre-formed backbones, and the subsequent decomposition to generate the desired oxide or metallic nano-catalysts[45-51]. This technique has shown many advantages in improving the electrode performance, such as lowering the resistance and mitigating the electrode degradation[51-55]. Lv *et al.* infiltrated GDC nanoparticles into SFM scaffold to form GDC-SFM nano-electrode for CO_2 electroreduction in SOECs, and found that the current density of the electrolyzer was enhanced from 0.283 to 0.446 Acm^{-2} after GDC infiltration at 1.6 V and 800 ^oC[56]. Rath *et al*. reported that the electrode polarization resistance could be significantly decreased while the electrochemical performance was effectively enhanced after introducing Pd or Co-Ni-Mo alloy nanoparticles into $Sr_2FeMoO_{6-\delta}$ skeleton[33]. In our previous work, it was found that the electrochemical performance of bare SFM-SDC electrode could be strongly improved by infiltrating Ni or Ru into SFM scaffold[31,32], and Ru infiltrated SFM-SDC electrode exhibited impressive electrochemical performance and good stability during partial oxidation methane assisted steam electrolysis operation[31]. Therefore, it is an efficient way to infiltrate metallic nanoparticles into the porous ceramic electrode scaffold to enhance the electrode performance. It is well-known that the electrode electrochemical performance is strongly associated with the microstructure of the electrode, which is greatly affected by the pre-sintering temperature and catalyst infiltration loading. Therefore, in this work, to better understand Ni infiltration effect on the evolution of microstructure and

electrochemical performance, the morphology of the SFM electrode before and after Ni infiltration is characterized by a scanning electron microscopy (SEM), while symmetrical cells with a cell configuration of Ni-SFM(SFM)/LDC/LSGM/LDC/Ni-SFM(SFM) are evaluated to determine the evolution of the electrode polarization resistance. Additionally, a newly developed numerical simulation of the 3D microstructure of Ni infiltrated SFM electrode is utilized to calculate the geometric parameters including effective triple phase boundaries (TPBs) and interface areas of Ni/SFM particles as functions of Ni infiltration loading and the radius of Ni nanoparticles, which will be used to explain the Ni infiltration effect in details. Finally, single cells with a cell configuration of Ni-SFM(SFM)/LDC/LSGM/LSCF-GDC are evaluated for power generation and CO_2 electrolysis applications.

2. Experimental

2.1 Powders synthesis

$Sr_2Fe_{1.5}Mo_{0.5}O_{6-\delta}$ (SFM) and $La_{0.5}Ce_{0.5}O_{1.75}$ (LDC) powders are synthesized using a glycine and citric acid assisted combustion method[31,32], while $La_{0.8}Sr_{0.2}Ga_{0.87}Mg_{0.13}O_3$ (LSGM) powders as well as LSCF-GDC slurry are purchased from FuelCellMaterials Inc. The details for the synthesis of SFM powders are described as follows: Stoichiometric amount of molybdate salt of $(NH_4)Mo_7O_{24}•7H_2O$ (Sigma-Aldrich, AR grade) is dissolved in deionized water. Citric acid, which acts as both the chelating agent and fuel for combustion, is then added into the molybdate salt solution with a molar ratio of 0.95:1 for citric acid to perovskite oxide. Stoichiometric amount of $Sr(NO_3)_2$ and $Fe(NO_3)_3•9H_2O$ (Sigma-Aldrich, AR grade) is then added to the above solution with a molar ratio of 2:1.5:0.5 for Sr:Fe:Mo. Glycine, the other chelating agent and fuel for combustion, is subsequently added to the above solution with a molar ratio of 10:1 for glycine: perovskite oxide.

The solution is then heated on a hot plate while under constant stirring until self-combustion occurs. The resulting ashes are collected and calcined at 1050 °C for 5 hours to obtain the perovskite oxide SFM powders.

2.2 Cell fabrication

Symmetrical cells composed of the LSGM electrolyte, LDC interlayers and SFM electrodes, are fabricated to investigate the effect of the pre-sintering temperature of SFM skeleton on the electrode polarization resistance[57,58], and the preparation process of the symmetrical cells is schematically shown in Figure 1. LSGM electrolyte with a diameter of 13 mm is firstly prepared by pressing the powders into pellets, followed by sintering at 1400 °C for 5 hours to densify the LSGM pellets. LDC interlayers are prepared by screen-printing the LDC slurry onto both sides of the dense LSGM electrolyte pellets and then sintering at 1200 °C for 2 hours to prevent the inter-reaction between the infiltrated Ni nanoparticles with the LSGM electrolyte. SFM electrodes are prepared by printing the SFM slurry onto both sides of the LDC interlayers and pre-sintering at 1000-1200 °C with an interval of 50 °C for 2 hours to determine the optimal pre-sintering temperature of the SFM skeleton. After obtaining the optimal SFM skeleton, Ni nanocatalysts are introduced by drop-depositing $Ni(NO_3)_2$ (Sigma-Aldrich, AR grade) solution to the SFM skeleton, which is subsequently dried and fired at 600 °C. Infiltration loadings of Ni nanoparticles are measured to be 0, 9.5 wt.%, 16.9 wt.%, and 26.0 wt.% compared to the bare SFM skeleton. Gold (Au) paste is then screen printed onto the SFM-based electrode as the current collector. The effective area of all the symmetrical cells is 0.82 cm^2. Both the SFM and the LDC slurries are prepared by ball-mixing ceramic powders, ethyl cellulose and α-terpineol with a weight ratio of 1:0.09:1.41.

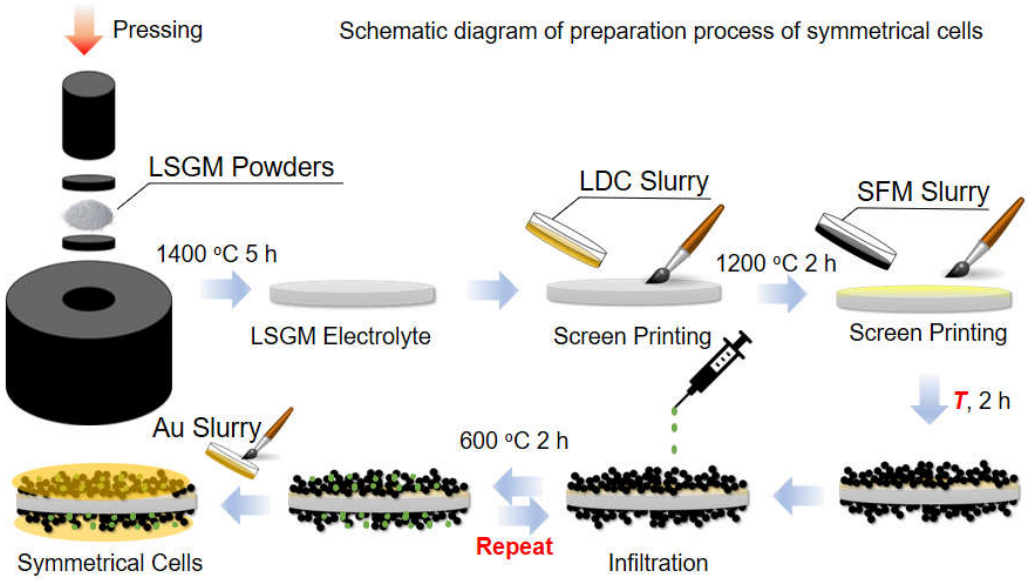

Figure 1 Schematic diagram of the preparation process of the symmetrical cells

Furthermore, single cells with the cell configurations of Ni-SFM/LDC/LSGM/LSCF-GDC and SFM/LDC/LSGM/LSCF-GDC are assembled for electrochemical performance evaluations[56]. The LSGM powers are dry-pressed and subsequently sintered at 1400 °C for 5 h to form the densified substrates. The LDC slurry is screen-printed on one side of the LSGM substrate and calcined at 1200 °C for 2h, and then the SFM slurry is printed on the surface of the LDC interlayer while the slurry containing LSCF-GDC composite materials is coated on the other side of the LSGM substrate to form SFM/LDC/LSGM/LSCF-GDC cell. Following, Ni nanocatalysts with a solid loading of 16.9 wt.% are infiltrated into the SFM skeleton via the ion-impregnated process mentioned in the above section to form Ni-SFM/LDC/LSCF-GDC cell. Gold (Au) paste is then screen-printed onto both sides of the cells as the current collector. The effective area of the single cells used in this work is 0.26 cm^2.

Note that the LSGM electrolyte pellets for both the single cells and symmetrical cells have the same thickness, and the value of the thickness is measured to be 575 μm.

137 2.3 Characterization

138 The introduction of Ni nanoparticles is examined by performing the X-ray diffraction (XRD,
139 PANalytical X'pert Pro), Raman spectra measurements (Renishaw RM-1000) and high resolution
140 transmission electron microscopy (HRTEM, Talos F200x, Thermo Fischer Scientific).
141 The cells morphology is observed by using scanning electron microscopes (SEM, MIRA3 LMH,
142 TESCAN & Ultra Plus FESEM, Zeiss), equipped with an energy dispersive spectrometer (EDS,
143 Maxx 100, Oxford Instruments).

144 Dense SFM bars with a dimension of 16×5×0.7 mm were prepared and measured by an electrical
145 conductivity relaxation method to investigate the effect of Ni infiltration on the surface oxygen
146 exchange co-efficient. The SFM and Ni infiltrated samples were first placed in a quartz tube with a
147 flowing 50%CO-50%CO_2 mixture (purchased from the gas company) at a rate of 200 $mLmin^{-1}$ to
148 achieve stability by recording the electrical conductivity with a relative change less than 0.5% within
149 20 min. Then the surrounding atmosphere was abruptly shifted from 50%CO-50%CO_2 to 67%CO-
150 33%CO_2 mixture. The normalized electrical conductivity relaxation plots were then fitted to obtain
151 the oxygen surface exchange coefficient k_{chem} as well as oxygen diffusion coefficient D_{chem} by using
152 a Matlab software. The fitting calculation is conducted at stepwise intervals over the proper range
153 of D and k, and the program ends when D and k come to the minimum discrepancy between the
154 calculated and experimental values.

155 The electrode polarization resistance (R_p) of bare SFM electrodes and Ni-infiltrated SFM
156 electrodes is measured on symmetrical cells in the reduced atmosphere, by exposing the samples in
157 hydrogen (3 vol% H_2O) with a gas flow rate of 30 mL min^{-1}. Impedance spectra of the symmetrical
158 cells are recorded at 600-800 °C in the frequency range from 0.01 to 1M Hz with a voltage amplitude

of 30 mV.

Electrochemical performances of the single cells with bare SFM and Ni infiltrated SFM electrodes were evaluated for both SOFC mode and high temperature CO_2 electrolysis process. When the cells were operated in the SOFC mode, the SFM or Ni-SFM electrode was fed with hydrogen (3 vol%H_2O), while the LSCF-GDC electrode was exposed to the ambient air. When the cells were operated for high-temperature CO_2 electrolysis mode, the gas composition in the SFM or Ni-SFM electrode was switched from hydrogen (3 vol%H_2O) to CO-CO_2 mixture ($CO:CO_2$ = 2:1, 1:1 and 1:2), and the flux of the feeding gas in the SFM/Ni-SFM electrode was maintained at 30 mL min^{-1} by using a precise digital mass flowmeter (APEX, Alicat Scientific). Current density-cell voltage (*i-V*) curves were recorded at a voltage scan rate of 30 mVs-1 to evaluate the power density in the SOFC mode and the electrolysis current density in the CO_2 electrolysis process. Electrochemical impedance spectra at open circuit voltage (OCV) condition were also carried out using an electrochemical workstation (Zennium E, Zahner) from 1 MHz to 0.1 Hz under a voltage amplitude of 30 mV.

2.4 Calculation

To better understand the Ni infiltration effect on the evolution of microstructure and electro-catalytic properties, the geometric properties of the electrodes are calculated as a function of Ni infiltration loading. Ni nanoparticle radius was determined by a numerical simulation of the 3D microstructure of infiltrated electrodes with the SFM backbone. The details of the simulation method can be found in our previous work[59,60].

3. Results and discussion

3.1. Phase structure and morphology

Figure 2a shows the XRD patterns of SFM powders before and after Ni infiltration. The bare SFM powders prepared by the glycine and citric acid assisted combustion method and calcined at 1050 °C for 5h show a single cubic perovskite crystalline structure (PDF# 34-0638) (Figure 2a), and exhibit homogenous morphology with a mean diameter of about 0.10±0.03 μm (Figure S1). After infiltrating $Ni(NO_3)_2$ solution, firing and reducing in 97%H_2-3%H_2O atmosphere, two extra peaks at 44.09 and 51.35 ° are observed and identified as Ni (PDF# 04-0850), suggesting that Ni has been successfully infiltrated into the SFM powders via ion-impregnation method. Meanwhile, Raman spectra of bare SFM electrode and Ni infiltrated SFM electrode are also collected and shown in Figure 2b. It can be found that only one peak at 834.0 cm^{-1} is observed for bare SFM electrode, however, two more peaks are observed at 447.7 and ~736.5 cm^{-1} for Ni infiltrated SFM electrode, which are consistent with the typical Raman peaks for metallic Ni phase previously reported[61], further confirming that Ni infiltrated SFM electrode has been successfully fabricated by introducing Ni into SFM skeleton via ion-impregnation technique. Additionally, the phase and structural information in further details are verified by HRTEM images (Figure 2c-g). It is clearly shown that some nanoparticles with a diameter of 20-30 nm are well-connected to the porous skeleton, and two representative lattice differences of 0.208 and 0.278 nm can be observed for the Ni infiltrated SFM powders, matching well with the distances for (111) for metallic Ni and (110) for perovskite oxide SFM, respectively. These results demonstrate that metallic Ni nanoparticles have been successfully infiltrated into SFM scaffold to form Ni infiltrated SFM powders (electrode) through solution infiltration.

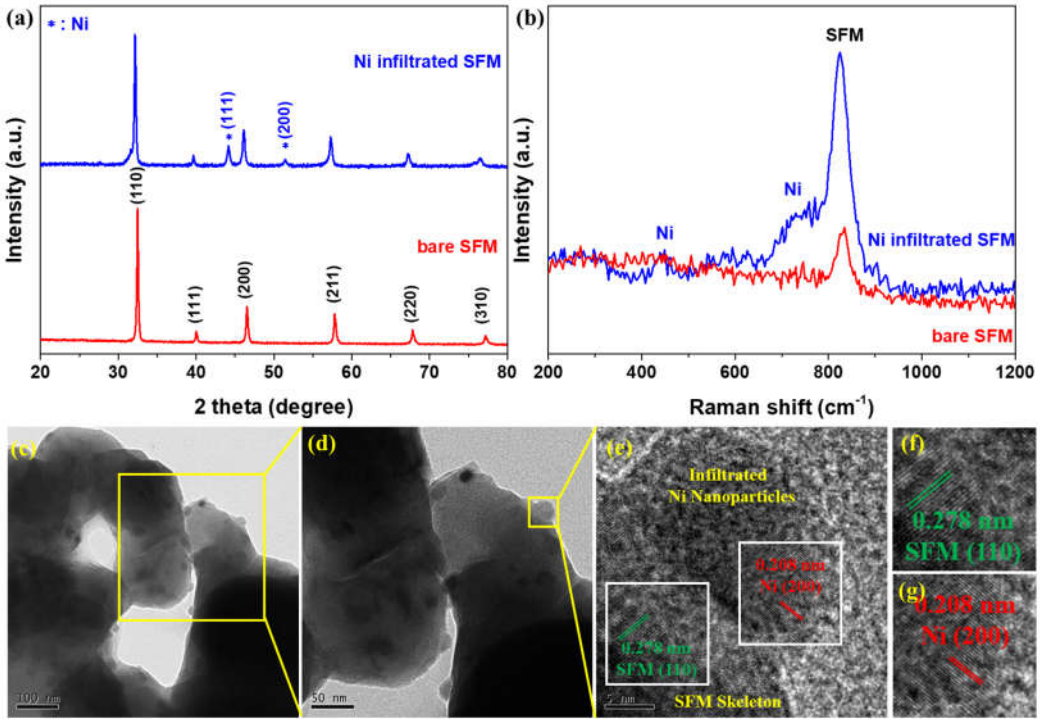

Figure 2 a) XRD patterns of SFM powders, b) Raman spectra of SFM electrodes of SFM powders before and after Ni infiltration, and c-g) HRTEM images of Ni infiltrated SFM powders, c-d) the overall image of Ni infiltrated SFM powders, e) the magnified HRTEM image marked in Figure 2d, f) and g) the magnified HRTEM images marked in green and yellow in Figure 2e, respectively.

3.2 Pre-sintering temperature effect

To achieve the optimal pre-sintering temperature for the preparation of SFM skeleton, five representative SFM skeletons have been prepared by pre-sintering at 1000, 1050, 1100, 1150, and 1200 °C for 2h, respectively, and the pre-sintering temperature effect on the microstructure evolution and the electrochemical performance of the bare SFM electrodes has been systematically studied by using SEM and electrochemical measurements. Figure 3 presents the area specific resistance (ASR or R_p) of the SFM electrodes measured at 600-800 °C in 3 vol.%H_2O-97 vol% H_2 atmosphere as a function of the pre-sintering temperature for the bare SFM skeletons. As can be seen from the inset in Figure 3a that the ASRs of the bare SFM electrodes are strongly affected by their pre-sintering

temperatures, and the ASR values measured at 800 °C are 2.20, 1.04, 1.50, 1.10, and 1.87 Ωcm^2 for the bare SFM electrodes pre-sintered at 1000, 1050, 1100, 1150, and 1200 °C, respectively. Additionally, the ASRs are greatly affected by the operating temperature, and significantly increased with lowering the operating temperature, which can be explained by the decreased electro-catalytic properties as well as the ionic conductivities of the SFM electrodes at lower operating temperature[62]. For example, when the operating temperature is reduced to 600 °C, the corresponding ASR values as shown in Figure 3a are significantly increased to 16.53, 6.94, 21.16, 25.01, and 21.53 Ωcm^2 for the bare SFM electrodes pre-sintered at 1000, 1050, 1100, 1150, and 1200 °C, respectively. It can be obviously seen that the SFM electrode pre-sintered at 1050 °C exhibits the lowest ASR values in all the operating temperature range of 600-800 °C, demonstrating that 1050 °C is the optimal pre-sintering temperature for the SFM electrode. To further evaluate the pre-sintering temperature effect on the electrochemical performance, the Arrhenius plots of the ASR values for the symmetrical cells pre-sintered at different temperatures are presented in Figure 3b. SFM electrode pre-sintered at 1050 °C demonstrates the lowest ASR than all the other samples at other pre-sintering temperatures. On the other hand, the activation energy for the SFM electrode pre-sintered at 1050 °C is calculated to be 0.320±0.017 eV, which is also lower than 0.341±0.005, 0.446±0.016, 0.531±0.025 and 0.390±0.028 eV for the samples pre-sintered at 1000, 1100, 1150, and 1200 °C, respectively, further indicating the superior performance of the SFM electrode pre-sintered at 1050 °C. In addition, it should be pointed out that although the ASR for the bare SFM electrode pre-treated at 1150 °C is close to that for SFM electrode pre-sintered at 1050 °C when operated at 800 °C, the values at lower operating temperature is much larger than those for the SFM electrode pre-sintered at 1050 °C, which can be confirmed by the larger activation energy for SFM

electrode pre-sintered at 1150 °C than that of the SFM electrode pre-sintered at 1050 °C. These results demonstrate that 1050 °C is the optimal pre-sintering temperature for the bare SFM electrode.

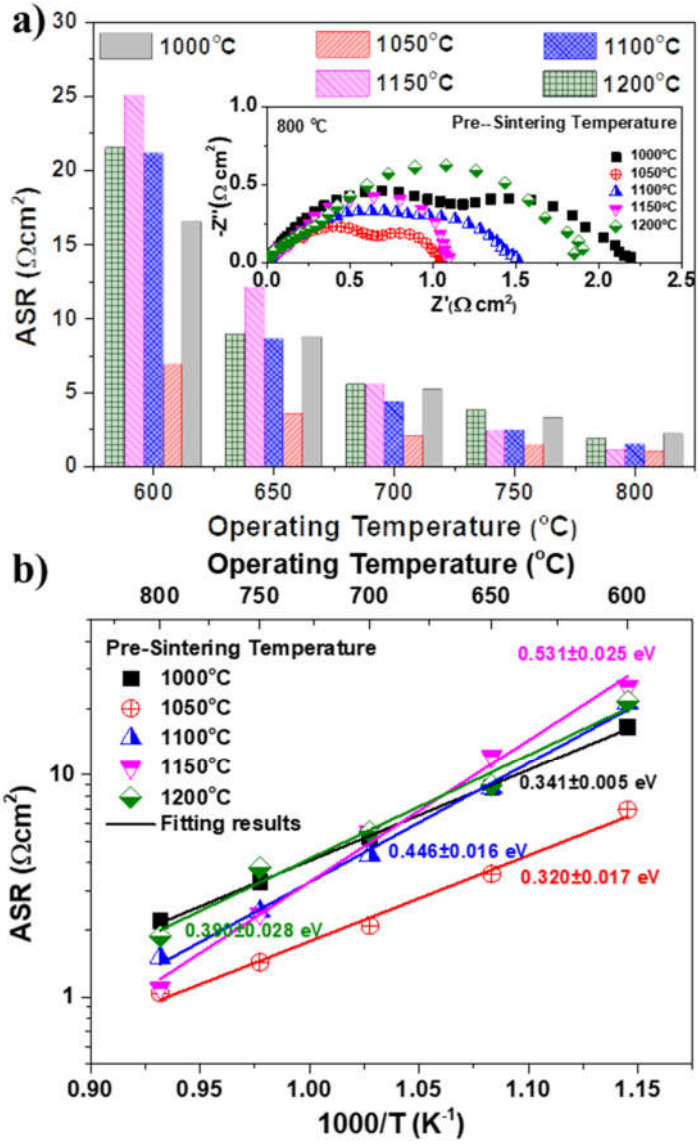

Figure 3 a) effects of operating temperature and pre-sintering temperature on the area specific resistances (ASR), and b) Arrhenius plots of the ASR for the SFM/LDC/LSGM/LDC/SFM symmetrical cells pre-sintered at 1000, 1050, 1100, 1150, and 1200 °C for 2h.

To better understand the correlation between the pre-sintering temperature and the evolution of the microstructure and electrochemical performance of the electrodes, the cross-sectional SEM

246 images of bare SFM electrodes (SFM scaffolds) calcined at 1000-1200 °C are characterized and
247 shown in Figure 4. It can be seen from Figure 4a-f that the feature size of SFM scaffold continually
248 increases with increasing the pre-sintering temperature from 1000 to 1200 °C. On the contrast, the
249 apparent porosity and the pore sizes of the SFM skeleton gradually decrease as the pre-sintering
250 temperature is raised from 1000 to 1200 °C. Table 1 summarizes the average feature size and
251 population distribution of SFM scaffold calculated by ImageJ software. The average feature size is
252 calculated to be 0.12±0.04 μm for the SFM scaffold pre-sintered at 1000 °C, which is very close to
253 the mean diameter (0.10±0.03 μm) of the as-prepared SFM powders calcined at 1050 °C for 5 h.
254 But the value is gradually increased to 0.31±0.14, 0.48±0.11, 0.79±0.28, and 1.24±0.31 μm with
255 increasing the pre-sintering temperature to 1050, 1100, 1150, and 1200 °C, respectively.
256 Additionally, the calculated population distribution of SFM particles is obviously decreased from
257 4.00 to 3.59, 2.77, 1.02, and 0.55 μm^{-2} when the pre-sintering temperature is increased from 1000
258 to 1050, 1100, 1150, and 1200 °C, respectively. It is well-known that smaller particles obtained at
259 lower pre-sintering temperature can provide more surfaces for oxygen exchange as well as electrode
260 reaction process to lower the activation resistance of the SFM electrode. At the same time, larger
261 porosity and pore sizes can benefit the gas transfer in the SFM electrode to effectively reduce the
262 concentration polarization resistance. These results demonstrate that low pre-sintering temperature
263 is preferred for the fabrication of the SFM skeleton. However, in contrast, it should be pointed out
264 that low pre-sintering temperature, such as 1000 °C in this work, may be not enough to make the
265 SFM skeleton well-connected to the LDC interlayer and the LSGM electrolyte (Figure 4g), which
266 can be confirmed by some observable large pores marked in Figure 4g (Figure S2a). But when the
267 pre-sintering temperature is increased to 1050 °C, the adhesion between the SFM electrode and LDC

interlayer/LSGM electrolyte may be effectively improved (Figure 4h), and no obvious large pores are detected for that pre-sintered at 1050 °C (Figure S2b). The morphology evolution induced by the pre-sintering temperature is consistent with the significantly enhanced electrochemical performance of bare SFM electrode after increasing the pre-sintering temperature from 1000 to 1050 °C (Figure 3). Therefore, in this work, 1050 °C is chosen as the pre-sintering temperature to prepare the SFM skeleton for Ni infiltration.

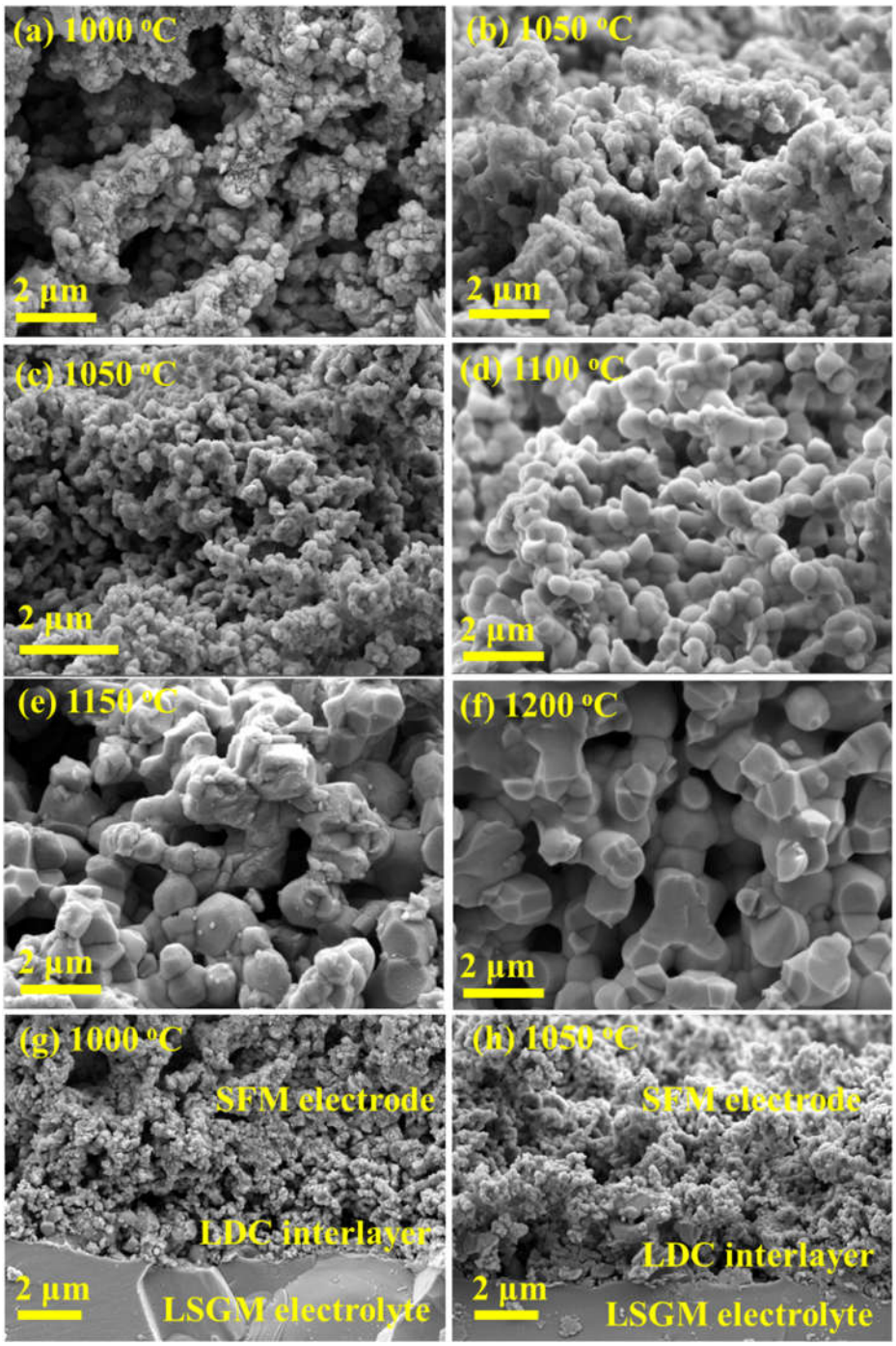

274

275 Figure 4 Cross-sectional SEM images of SFM skeleton calcined at (a) 1000 °C, (b-c) 1050 °C, (d) 1100

276 °C, (e) 1150 °C, and (f) 1200 °C, and cross-sectional SEM images of SFM/LDC/LSGM/LDC/SFM

277 symmetrical cells calcined at (g) 1000, and (h) 1050 °C.

278

279 Table 1 Calculated average feature size and population distribution of SFM scaffolds pre-sintered at

280 different temperatures

Pre-Sintering Temperature (°C)	Average Feature Size (μm)	Population Distribution (μm^{-2})
1000	0.12±0.04	4.00
1050	0.31±0.14	3.59
1100	0.48±0.11	2.77
1150	0.79±0.28	1.02
1200	1.24±0.31	0.55

281

282 3.3 Ni infiltration loading effect

283 Figure 5 summarizes the effect of Ni infiltration loading on ASRs measured at 600-800 °C. It can

284 be seen from Figure 5a that the ASR of the electrode has been significantly decreased after Ni

285 infiltration. For example, the electrode polarization resistance measured at 800 °C is significantly

286 reduced from 1.04 Ωcm^2 for the bare SFM electrode to 0.46, 0.32, 0.35 Ωcm^2 for the SFM electrode

287 infiltrated with 9.45 wt.%, 16.9 wt.%, and 26.0 wt.% Ni nanocatalysts, and the largest enhancement

288 of 225% is achieved for 16.9 wt.% Ni infiltrated SFM electrode. Additionally, when the operating

289 temperature is lowered to 600, 650, 700, and 750 °C, the electrode polarization resistance can be

290 greatly decreased from 6.75, 3.56, 2.09, 1.43 to 2.61, 1.24, 0.68, 0.44 Ωcm^2 as 16.9 wt.% Ni

291 nanoparticles are introduced into the SFM scaffold, demonstrating a significant improvement in

292 electrochemical performance of the SFM based electrode with an enhancement larger than 187%.

293 These results indicate that Ni infiltration is an effective way to enhance the electrochemical

294 performance of the SFM electrode. In addition, the Arrhenius plots of the ASR for the

SFM/LDC/LSGM/LDC/SFM symmetrical cells infiltrated with different Ni loadings are presented in Figure 5b. It is clearly shown that the electrode polarization resistances have been strongly reduced after Ni infiltration, but no obvious changes in the activation energy is observed. As the Ni infiltration loading is increased from 0 to 9.5 wt.%, the activation energy is decreased from 0.320±0.017 to 0.286±0.017 eV, but then increased to 0.357±0.020, and 0.333±0.007 eV as the infiltration loading is further increased to 16.9 wt.%, and 26.0 wt.%, respectively. The decreased activation energy after Ni infiltration is possibly attributed to the increased active electrochemical reaction sites for hydrogen oxidation, however, the excess infiltrated Ni nanoparticles may block the gas transport in the electrode, leading to an increased activation energy.

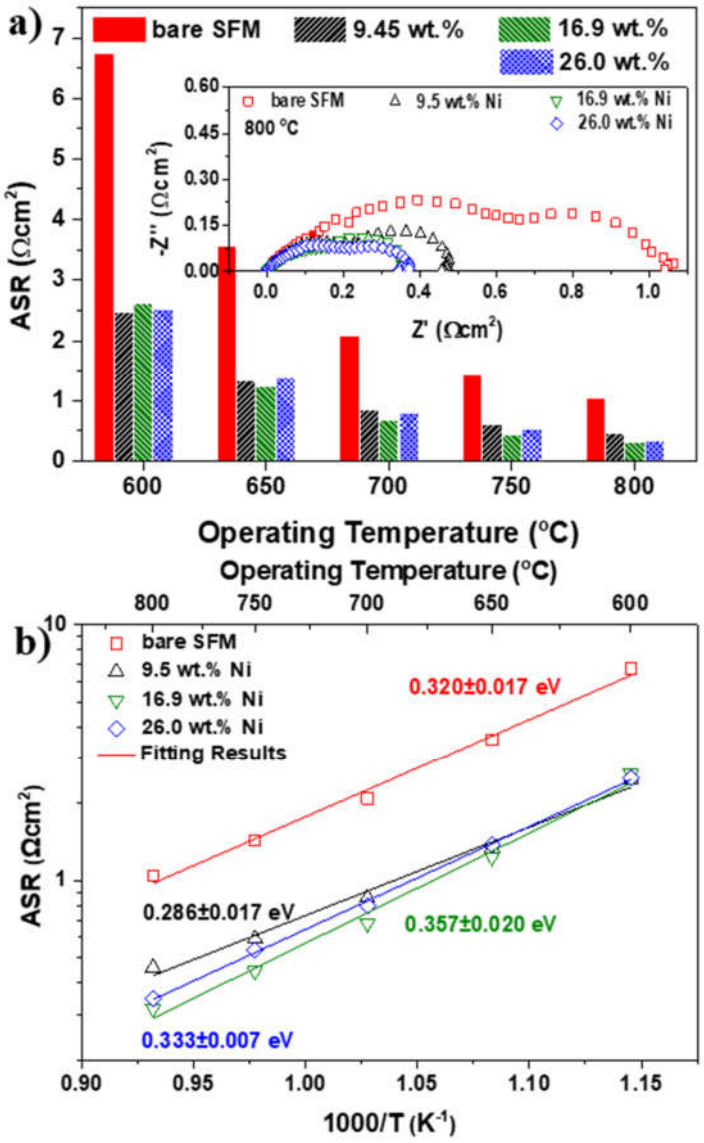

Figure 5 a) effects of operating temperature and infiltration loading on the ASR, and b) Arrhenius plots of the ASR for the SFM/LDC/LSGM/LDC/SFM symmetrical cells infiltrated with different Ni loadings.

To better understand the Ni infiltration loading effect on the electrode microstructure and more clearly correlate the microstructure and electrochemical performance of the electrodes, the cross-sectional SEM images of the infiltrated SFM electrodes with different Ni infiltration loadings are collected and shown in Figure 6. At low Ni loading of 9.5 wt.%, the hemispheric Ni nanoparticles with a diameter of 23±4 nm are homogeneous and well-dispersive onto the inner surface of the

312 porous SFM scaffold (Figure 6(a-b)). Meanwhile, as shown in Figure 6(c-d), with increasing the Ni
313 infiltration loading to 16.9 wt.%, the diameter of the infiltrated Ni nanoparticles is increased to about
314 78±15 nm, and further to approximate 97±20 nm as the infiltration loading is increased to 26.0 wt.%.
315 In addition, it is also found that some rod-like Ni nanoparticles instead of hemispheric structure are
316 observed at high infiltration loading of 26.0 wt.%, which may reduce the effective reaction sites for
317 electrode reaction process at high infiltration loading and result in an increased ASR. At the same
318 time, the cross-sectional SEM image as well as the line element distribution of the interface of 16.9
319 wt.% Ni infiltrated SFM electrode and LSGM electrode is observed by using SEM equipped with
320 EDS sensor and shown in Figure 6(e-f). As depicted in EDS image measured in line-scan mode
321 (Figure 6(f)), seven representative elements including La, Sr, Ga, Fe, Ce, Ni, and O can be observed,
322 and these elements can be divided into three groups: La and Ga elements in the left issued from
323 LSGM electrolyte, La and Ce elements in the middle originated from LDC interlayer, while Sr, Ni
324 and Fe elements in the right assigned to Ni-SFM electrode, indicating that three distinctive layers
325 can be detected and determined as LSGM electrolyte, LDC interlayer, and Ni-SFM electrode.
326 respectively. It is also found that no obvious diffusion between Ni element and Ga element can be
327 observed, indicating that LDC interlayer can effectively prevent the reaction between Ni-SFM
328 electrode and LSGM.

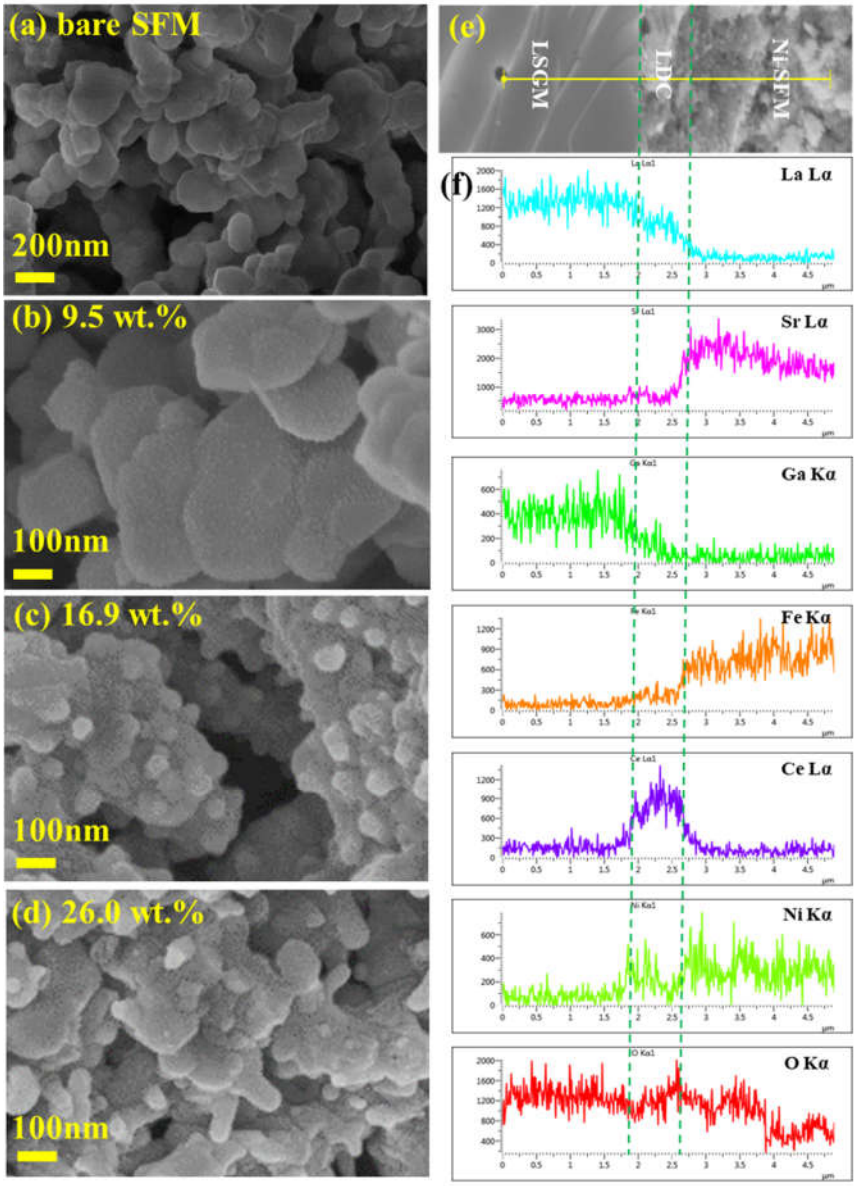

Figure 6 Cross-sectional SEM images of SFM electrodes infiltrated with different Ni loadings, (a) bare SFM, (b) 9.5 wt.%, (c) 16.9%, and (d) 26.0 wt.%, (e) cross-sectional SEM image and (f) EDS image in line scan mode of the interface of Ni-SFM/LDC/LSGM.

It is well-known that the electro-catalytic properties of the electrode materials as well as their corresponding electrochemical performance are strongly associated with the surface exchange processes of the electrodes, which can be accurately evaluated by the electrical conductivity relaxation (ECR) measurement through the normalized conductivities as a function of the elapsed

time[63-66]. Figure 7 shows the normalized conductivities as a function of the elapsed time measured at 800 °C for the SFM samples before and after Ni infiltration. With the surrounding atmosphere shifting from 50%CO-50%CO_2 to 67%CO-33%CO_2, the re-equilibrium time has been reduced from 7500 s for bare SFM sample to 900 s for Ni infiltrated SFM sample. The oxygen diffusion coefficient, D_{chem}, determined by the ECR method, is fitted to be 9.0×10^{-6} cm^2s^{-1} for both SFM and Ni infiltrated SFM samples. On the contrast, the surface oxygen exchange coefficient, k, has been significantly accelerated by more than one order of magnitude from 1.5×10^{-5} cms^{-1} for bare SFM sample (k_{SFM}) to 2.4×10^{-4} cms^{-1} for Ni infiltrated SFM sample ($k_{Ni\text{-}SFM}$), demonstrating that the kinetics of surface exchange steps of the SFM electrode and the electrochemical performance of the cells can be greatly promoted by introducing highly active Ni nanoparticles.

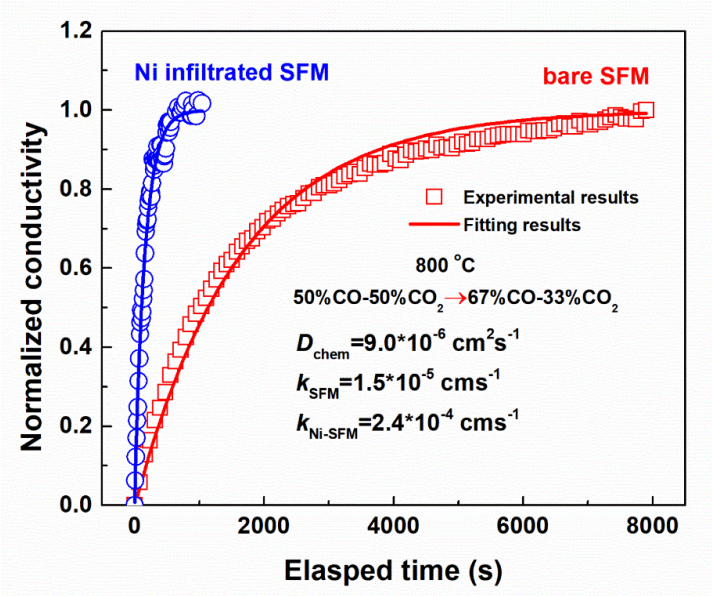

Figure 7 Normalized conductivity relaxation plots of the SFM bar samples as a function of elapse time before and after Ni infiltration.

3.4 Simulated 3D microstructure of infiltrated electrodes

It is reported that the electrode electrochemical performance is not only greatly affected by the

352 total and percolated TPB length, but also strongly associated with the total and percolated surface
353 area of electro-catalytic phase as well as the porosity of the electrode[59]. However, it is difficult to
354 determine these geometric parameters by using the conventional experimental methods, especially
355 when the particle size and particle shape are significantly varied as a result from the different
356 infiltration loadings. Therefore, to better determine the Ni infiltration effect on the evolution of
357 microstructure and electro-catalytic properties, the geometric properties of the electrodes are
358 calculated as functions of the infiltration loading and nanoparticle radius through numerical
359 simulation of the 3D microstructure of the Ni infiltrated electrodes with the SFM backbone.
360 According to the experimental results (Figure 4), the SFM backbone can be idealized as a random
361 packing system of spherical particles (with a radius of ~300 nm, simplified from 0.31±0.14 μm for
362 SFM scaffold pre-sintered at 1050 ^{o}C, a porosity of ~37.6vol%, and a contacting angle of ~60 ^{o} for
363 mimicking sintering effect). The bare backbone is then simulated using our previous method[67],
364 and is defined as a baseline condition. The simulated Ni nanoparticles with a diameter of 25, 75, or
365 100 nm, which are very close to the calculated value of 23±4, 78±15, and 97±20 nm for the electrodes
366 with different Ni loadings, respectively, are then infiltrated numerically into the SFM backbone.
367 Figure 8 shows the simulated 3D microstructure of the SFM electrodes with different Ni infiltration
368 loadings under the baseline condition. The red particles shown in Figure 8 represent the SFM
369 scaffold, while the green particles shown in Figure 8b-d indicate infiltrated Ni nanoparticles. The
370 parametric study is presented at follows.

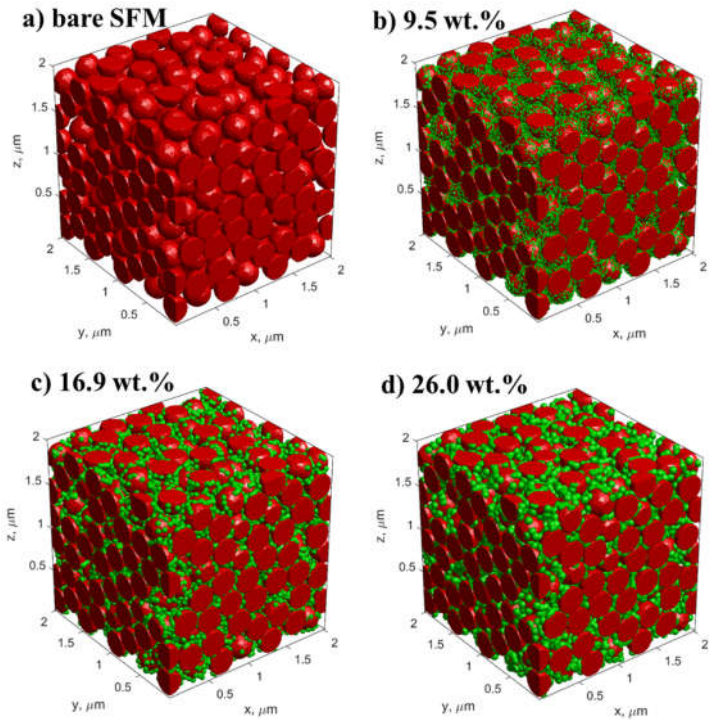

Figure 8 Three-dimensional visualization of the baseline structure with Ni infiltration loadings of a) 0, b) 9.5 wt.%, c) 16.9 wt.%, and 26.0 wt. %. (Backbone porosity = 37.6 vol.%, r_{SFM}=300 nm, r_{Ni} = 20, 75, and 100 nm calculated from Figure 6 for Ni infiltration loading of 9.5 wt.%, 16.9 wt.%, and 26.0 wt. %, respectively)

Figure 9 shows the length of total and percolated three phase boundaries (TPBs) of SFM/Ni/pores as a function of infiltration loading at different sizes of the infiltrated Ni nanoparticles (20, 75, and 100 nm). As shown in Figure 9a, there exists a threshold infiltration loading at 6.85 wt.%, 11.0 wt.%, and 15.6 wt.% for the infiltrated Ni nanoparticles with a diameter of 20, 75, and 100 nm, respectively, while their optimal Ni infiltration loadings, corresponding to the peak percolated TPBs length, are calculated to be 16.8 wt.%, 20.7 wt.% and 27.5 wt.%. According to the numerical simulation, the effective percolated TPBs length for Ni infiltrated SFM electrodes reported in this work is calculated to be 0, 152.5, 83.4, and 46.3 μm μm^{-2} for the SFM electrodes with Ni infiltration loading of 0, 9.5 wt.%, 16.9 wt.% and 26.0 wt.%, respectively. At the same time, the surface area of Ni particles

385 ($Area_{EPS}$) and interfacial area of SFM/Ni interface ($AreaP_{EPS}$), where electrochemical reaction such
386 as CO_2 reduction or hydrogen oxidation process possibly occurs, are also calculated and presented
387 in Figure 9b, indicating that $Area_{EPS}$ and $AreaP_{EPS}$ are both strongly affected by Ni infiltration
388 loading and Ni nanoparticle size, and smaller Ni particles will lead to higher $Area_{EPS}$ and $AreaP_{EPS}$.
389 After introducing 9.5 wt.% Ni nanoparticles with a diameter of 20 nm into the porous SFM skeleton,
390 $Area_{EPS}$ can reach 7.74 $\mu m^2\ \mu m^{-3}$. However, as the Ni infiltration loading is further increased to 16.9
391 wt.% and 26.0 wt.%, $Area_{EPS}$ is gradually decreased to 6.17 and 4.64 $\mu m^2\ \mu m^{-3}$, respectively, which
392 is caused by the significantly grown Ni nanoparticles as is verified experimentally in Figure 6. On
393 the contrast, $AreaP_{EPS}$ is gradually increased from 2.04 to 2.48 and 2.79 $\mu m^2\ \mu m^{-3}$ as the infiltration
394 loading is increased from 9.5 wt.% to 16.9 wt.% and 26.0 wt.%, respectively. It should be pointed
395 out that the porosity of SFM electrode is decreased after Ni infiltration because the infiltrated Ni
396 nanoparticles will attach on the surfaces of the SFM skeleton, and occupy the pores in the SFM
397 electrode. Therefore, the decrease of the porosity is equal to the increase of the volume of Ni
398 nanoparticles. According to the densities of SFM (5.59 g cm^{-3}) and Ni (8.90 g cm^{-3}), the volume
399 percentage of infiltrated Ni nanoparticles, equivalent to the decrease of the porosity, is calculated to
400 be 6.0 vol.%, 10.6 vol.%, and 16.3 vol.% for the SFM electrodes with Ni infiltration loading of 9.5
401 wt.% to 16.9 wt.% and 26.0 wt.%, respectively. The original porosity for the five parallel bare SFM
402 electrode pre-sintered at 1050 °C, a critical parameter for the numerical calculation, is determined
403 to be 37.6±1.0 vol.% by using Archimedes method in water. The porosity values for the Ni infiltrated
404 SFM specimen is calculated to 31.6 vol.%, 27.0 vol.%, and 21.3 vol.% after Ni infiltration loading
405 of 9.5 wt.% to 16.9 wt.% and 26.0 wt.% by dividing the Ni infiltration loading to Ni density,
406 respectively (Figure 9c). Since the concentration polarization is strongly affected by the porosity of

the electrode, reduction in porosity is expected to lead to increased polarization resistance, thus lowering the electrode electrochemical performance.

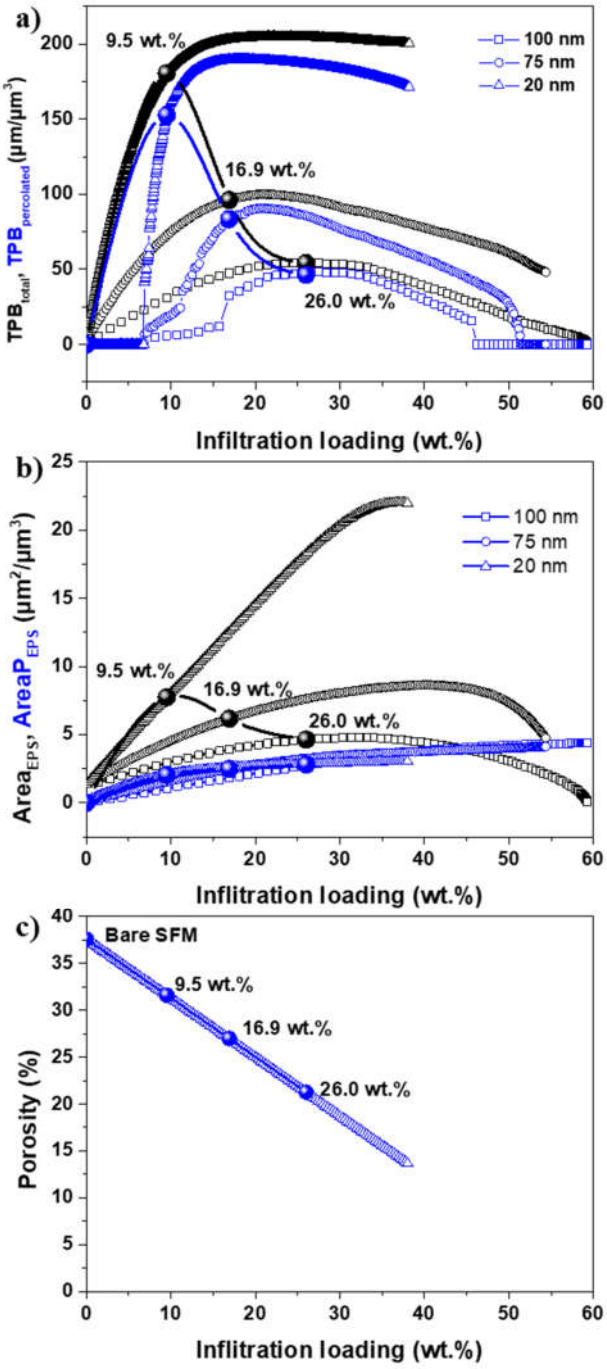

Figure 9 a) Total and percolated three-phase boundary length, b) surface area of Ni particles and interface area of SFM particles and Ni particles, and c) porosity of the electrode as a function of

412 infiltration loading of Ni nanoparticles. Backbone porosity = 37.6 vol.%, r_{SFM}=300 nm, r_{Ni} = 20, 75,
413 and 100 nm for Ni infiltration loading of 9.5 wt.%, 16.9 wt.%, and 26.0 wt. %, respectively.
414 In order to better explain Ni infiltration loading effect on the electrochemical performance, the
415 experimental results including R_p, effective percolated TPBs length, $Area_{EPS}$, $AreaP_{EPS}$ and porosity
416 of Ni infiltrated SFM electrodes are summarized in Figure 10. It can be seen that the 9.5 wt.% Ni
417 infiltrated SFM electrode, which has the largest percolated TPBs length, AreaEPS, and porosity, but
418 lowest $AreaP_{EPS}$, exhibits the worst electrochemical performance, while the 26.0 wt.% Ni infiltrated
419 SFM electrode, having the highest $AreaP_{EPS}$, but the smallest percolated TPBs length, $Area_{EPS}$, and
420 porosity, demonstrates much more improved electrochemical performance than the 9.5 wt.% Ni
421 infiltrated SFM electrode. As it is well known that the activation resistance, a component of R_p is
422 strongly associated with percolated TPBs length, $Area_{EPS}$ and $AreaP_{EPS}$, while the concentration
423 resistance, another component of R_p, is greatly affected by the porosity of the electrode and strongly
424 increased with lowering the porosity of the electrode. These results demonstrate that the weight of
425 $AreaP_{EPS}$ for the entire electrode reaction process is larger than the others. At the same time, it cannot
426 be neglected that the SFM electrode with Ni infiltration loading of 16.9 wt.%, which possesses
427 moderate percolated TPBs length, $Area_{EPS}$, $AreaP_{EPS}$ and porosity, yields the minimum R_p and
428 demonstrates better electrode electrochemical performance than the electrode with higher
429 infiltration loading and larger $AreaP_{EPS}$, indicating that the electrochemical performance of the Ni
430 infiltrated SFM electrode is also influenced by the percolated TPBs length, AreaEPS and porosity.
431 Consequently, it can be concluded from the experimental and numerical results that the metallic
432 nanoparticles infiltrated perovskite oxide electrode is primarily affected by the interfacial areas
433 between the infiltrated metallic phase and scaffold phase, and also influenced by other geometric

parameters including the percolated TPBs length, surface area of the infiltrated metallic phase and the porosity of the scaffold.

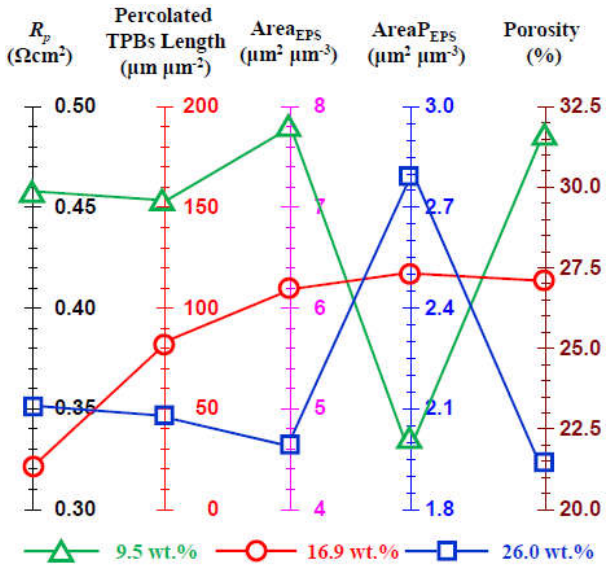

Figure 10 Various characteristics of Ni infiltrated SFM electrodes with different Ni infiltration loadings shown in Figure 5, 6 and 9, plotted in a parallel coordinate system (errors are smaller than the points).

3.5 Electrochemical performance of single cells

To further evaluate the electrochemical performance of the cells with SFM electrode before and after Ni infiltration, electrolyte-supported cells with different configurations of SFM/LDC/LSGM/LSCF-GDC and Ni-SFM/LDC/LSGM/LSCF-GDC are prepared for power generation (SOFC mode) and CO_2 electrolysis (SOEC mode). Typical *i-V* and *i-p* polarization curves are measured and shown in Figure 11 by operating these two types of cells in the SOFC mode at 700-800 °C with 40 mL cm^{-2} humidified H_2 (3 vol.% H_2O) as the fuel and static ambient air as the oxidant. The OCVs at the temperature from 700 to800 °C are higher than 1.0 V, indicating that the cells are well sealed with no gas leakage during operation. In addition, no concentration polarization is observable at high current density during the operation for both types of cells,

suggesting the porosity of the electrodes is sufficient for effective gas diffusion after 16.9 wt.% Ni infiltration. The cell performance has been remarkably enhanced after Ni infiltration, as presented in Figure 11b. The peak power density (P_{max}) of the bare SFM electrode is 0.106, 0.178, and 0.259 W cm^{-2}, respectively, which has been increased to 0.133, 0.278, and 0.361 W cm^{-2} at 700, 750, and 800 ^{o}C, respectively, after introducing Ni nanoparticles. EIS are also measured under OCV conditions for these two types of cells and shown in Figure 11c. For simplification, the ohmic resistance (R_{ohmic}), which corresponds to the first intercept of the impedance spectra with the x-axis, has been removed to reveal the electrode polarization resistance (R_p). It is found that R_p is effectively decreased from 0.467 to 0.357 Ωcm^2 at 800 ^{o}C after Ni infiltration, indicating that the electrode reaction process is significantly accelerated by introducing Ni nanoparticles. Meanwhile, the electrode polarization resistance is decreased from 0.924 to 0.528, and 0.357 Ωcm^2 with increasing the operating temperature from 700 to 750, and 800 ^{o}C, respectively, because of the greatly enhanced electro-catalytic properties of the electrode as well as increased oxygen ionic conductivity at higher operating temperature[51-53].

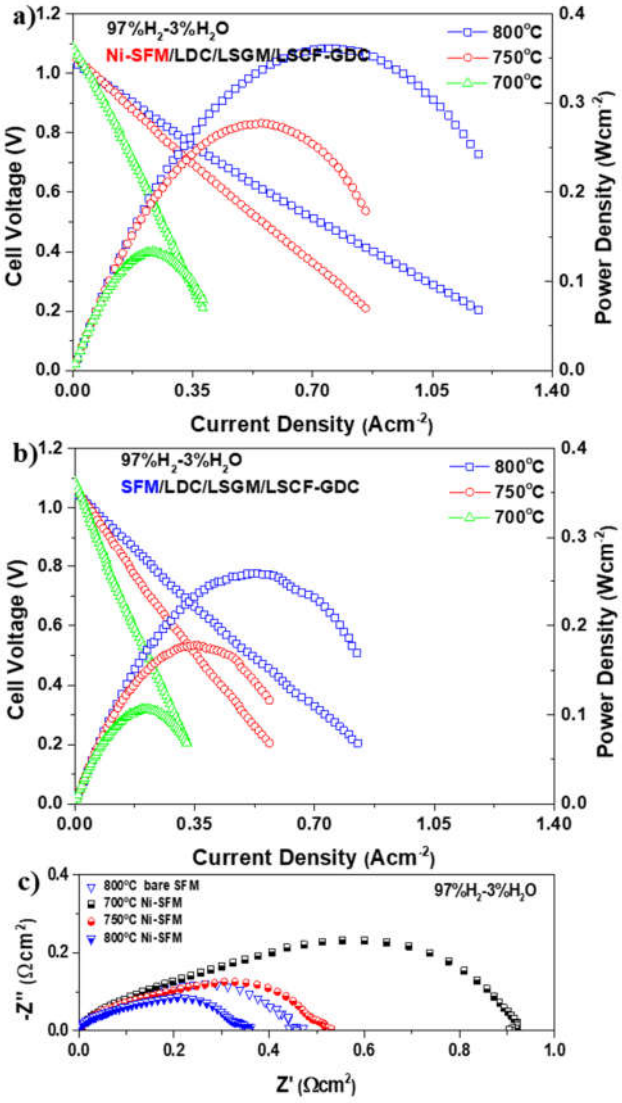

Figure 11 Typical *i-V* and *i-p* polarization curves of the electrolyte-supported cells with the configurations of a) Ni-SFM/LDC/LSGM/LSCF-GDC, and b) SFM/LDC/LSGM/LSCF-GDC, and c) EIS of the above-mentioned two single cells.

To further investigate the effect of Ni infiltration on electrochemical performance, cells using bare and Ni infiltrated SFM electrode are also operated for CO_2 electrolysis process. Figure 12a-b shows the typical *i-V* curves of the cells exposed to 67%CO_2-33%CO atmosphere. An electrolysis current density of 0.745 Acm^{-2} is obtained at 800 °C at 1.6V for cells with a configuration of SFM/LDC/LSGM/LSCF-GDC, and the electrolysis current density is increased to 1.070 Acm^{-2} after

473 the introduction of Ni nanoparticles, which is about 43.6% higher than the electrolyzer with GDC
474 infiltrated SFM as the electrode at the similar testing condition (0.446 Acm^{-2} @ 1.6 V, 800 ^oC)[56].
475 At the same time, it is also observed that R_p is decreased from 0.850 to 0.759 Ωcm^2 (Figure 12c),
476 which is in good agreement with the improved electrochemical performance. These results confirm
477 that Ni infiltration is an efficient way to enhance the cell performance due to the increased active
478 reaction sites for the electrode reaction. The electrochemical performance of Ni infiltrated cells for
479 CO_2 electrolysis are also investigated under another two gas compositions with lower CO_2
480 concentration. As the feeding gas is shifted from 67%CO_2-33%CO to 50%CO_2-50%CO, and
481 33%CO_2-67%CO, the electrolysis current density is decreased from 1.070 to 0.841, and 0.699 Acm^{-2}
482 (Figure 12a), which is ascribed to the decreased effective TPBs induced by the lowered reactive
483 gas CO_2 fraction in the Ni-SFM electrode.

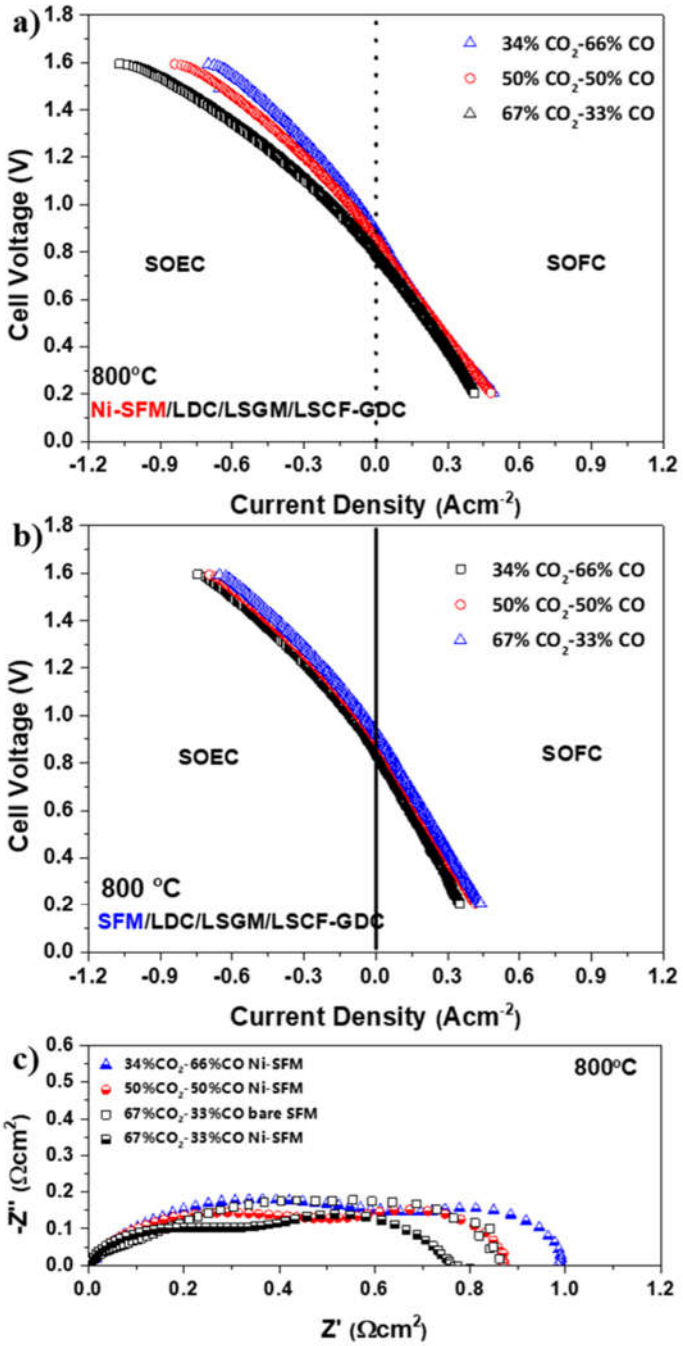

484

485 Figure 12 Typical *i-V* curves of the electrolyte-supported cells with the configurations of (a) Ni-

486 SFM/LDC/LSGM/LSCF-GDC and (b) SFM/LDC/LSGM/LSCF-GDC, and (c) EIS of the above-

487 mentioned two single cells measured at OCV conditions.

488

489

4. Conclusions

In this work, bare and Ni-infiltrated SFM electrodes have been prepared, and the correlation between fabrication processing parameters, the microstructure and electrochemical performance of the electrodes has been investigated. 1050 ^{o}C has been found to be the optimal pre-sintering temperature of the SFM scaffold, and the lowest R_p of 1.04 Ω cm^2 is obtained at 800 ^{o}C in hydrogen (3 vol.% H_2O) atmosphere for the non-infiltrated symmetrical cells pre-fired at 1050 ^{o}C. Moreover, the electrode is significantly activated after Ni infiltration, and the R_p value is greatly reduced to 0.32 Ω cm^2 at the Ni infiltration loading of 16.9 wt.% at 800 ^{o}C in hydrogen (3 vol.% H_2O) atmosphere. Geometric properties such as effective TPBs and interfacial areas have been calculated by numerically simulating the 3D microstructure evolution of the bare and Ni-infiltrated SFM electrode. It is found that metallic nanoparticles infiltrated perovskite oxide electrode is primarily dominated by the effective interfacial areas between the infiltrated metallic phase and scaffold phase ($AreaP_{EPS}$), where the fuel oxidation reaction occurs. At the same time, the electrode electrochemical performance is also influenced by other geometric parameters including the percolated TPBs length, surface area of the infiltrated metallic phase ($Area_{EPS}$) and the porosity of the electrode. These results indicate that it is critical to increase the effective interfacial areas ($AreaP_{EPS}$) to effectively enhance the performance of the metallic phase infiltrated electrode.

Acknowledgements

This work was supported by National Natural Science Foundation of China (51602228, 51502207, 21673062, 51402066), National Key R&D Program of China (2017YFA0700104), Natural Science Foundation of Hubei Province of China (2016CFB243, 2017CFB655), the China Postdoctoral

Science Foundation (2016M590712, 2017T100575), the 111 Project (D17003), and the U.S. National Science Foundation (1832809).

Statement of Contributions

T. L, Y. W. and Y. Z. conceived and supervised the project. J. X. synthesized the materials, fabricated the cells, and performed electrochemical performance. S. W. conducted the simulated results. All the authors (J. X., S. W., Y. W., S. H., Z. Y., F. C., Y. Z., and Y. W.) analyzed the experimental results and wrote the manuscript.

References

[1] Bi L, Boulfrad S, Traversa E, Steam electrolysis by solid oxide electrolysis cells (SOECs) with proton-conducting oxides. *Chem Soc Rev* 2014; 43: 8255-8270. https://doi.org/10.1039/C4CS00194J

[2] Xie Y, Shi N, Hu X, Liu M, Yang Y, Huan D, Pan Y, Peng R, Xia C, Novel in-situ MgO nano-layer decorated carbon-tolerant anode for solid oxide fuel cells, *Int J Hydrogen Energy* 2020; 45: 11791-11801 . https://doi.org/10.1016/j.ijhydene.2020.02.117

[3] Hauch A, Küngas R, Blennow P, Hansen A B, Hansen J B, Mathiesen B V, Mogensen M B, Recent advances in solid oxide cell technology for electrolysis, *Science*, 2020, 370(6513): eaba6118. https://doi.org/10.1126/science.aba6118

[4] Wachsman ED, Lee KT, Lowering the temperature of solid oxide fuel cells. *Science* 2011; 334: 935-939. https://doi.org/10.1126/science.1204090

[5] Huang Y-H, Dass R I, Xing Z-L, Goodenough J B, Double perovskites as anode materials for solid-oxide fuel cells. *Science* 2006; 312(5771): 254-257. https://doi.org/ 10.1126/science.1125877

[6] Li Y, Na L, Lü Z, Li S, Sulfur poisoning and the regeneration of the solid oxide fuel cell with metal catalyst-impregnated $La_{0.75}Sr_{0.25}Cr_{0.5}Mn_{0.5}O_{3-\delta}$ anode, *Int J Hydrogen Energy* 2020; 45: 15650-15657. https://doi.org/10.1016/j.ijhydene.2020.04.050

[7] Duan C, Kee R J, Zhu H, Karakaya C, Chen Y, Ricote S, Jarry A, Crumlin E J, Hook D, Braun R, Sullivan N P, O'Hayre R, Highly durable, coking and sulfur tolerant, fuel-flexible protonic ceramic fuel cells. Nature, 2018; 557: 217-222. https://doi.org/10.1038/s41586-018-0082-6

[8] Wang Y, Xia C, Nano-structural effect on SOFC durability. In: Leung DY, Xuan J, editors. Micro & Nano-Engineering of Fuel Cells, EH Leiden, The Netherlands: CRC Press, 2015, pp.181-210.

[9] Monzón H, Laguna-Bercero MA, Redox-cycling studies of anode-supported microtubular solid oxide fuel cells, *Int J Hydrogen Energy* 2012; 37: 7262-7270. https://doi.org/10.1016/j.ijhydene.2011.10.026

[10] Sarantaridis D, Chater RJ, Atkinson A, Changes in physical and mechanical properties of SOFC Ni–YSZ composites caused by redox cycling. *J Electrochem Soc* 2008; 155: B467-B472. https://doi.org/10.1149/1.2883731

[11] Jiao Z, Shikazono N, Kasagi N, Quantitative characterization of SOFC nickel-YSZ anode microstructure degradation based on focused-ion-beam 3D-reconstruction technique. *J Electrochem Soc* 2012; 159: B285-B291. https://doi.org/10.1149/2.045203jes

[12] Chen H-Y, Yu H-C, Scott Cronin J, Wilson JR, Barnett SA, Thornton K, Simulation of coarsening in three-phase solid oxide fuel cell anodes. *J Power Sources* 2011; 196: 1333-1337. https://doi.org/10.1016/j.jpowsour.2010.08.010

[13] Shen C-T, Lee Y-H, Xie K, Yen C-P, Huang J-W, Lee K-R, Lee S-W, Tseng C-J, Correlation between microstructure and catalytic and mechanical properties during redox cycling for Ni-BCY and

Ni-BCZY composites. *Ceram Int* 2017; 43: S671-S674. https://doi.org/10.1016/j.ceramint.2017.05.250

[14] Liu Q, Dong X, Xiao G, Zhao F, Chen F, A novel electrode material for symmetrical SOFCs. *Adv Mater* 2010; 22: 5478-5482. https://doi.org/10.1002/adma.201001044

[15] Bernadet L, Moncasi C, Torrell M, Tarancón A, High-performing electrolyte-supported symmetrical solid oxide electrolysis cells operating under steam electrolysis and co-electrolysis modes. *Int J Hydrogen Energy* 2020; 45(28): 14208-14217. https://doi.org/10.1016/j.ijhydene.2020.03.144

[16] Meng X, Wang Y, Zhao Y, Zhang T, Yu N, Chen X, Miao M, Liu T, In-situ exsolution of nanoparticles from Ni substituted $Sr_2Fe_{1.5}Mo_{0.5}O_6$ perovskite oxides with different Ni doping contents. *Electrochim Acta* 2020; 438: 136351. https://doi.org/10.1016/j.electacta.2020.136351

[17] Wang Y, Lei X, Zhang Y, Chen F, Liu T, In-situ growth of metallic nanoparticles on perovskite parent as a hydrogen electrode for solid oxide cells. *J Power Sources* 2018; 405: 114-123. https://doi.org/10.1016/j.jpowsour.2018.10.023

[18] Du Z, Zhao H, Yi S, Xia Q, Gong Y, Zhang Y, Cheng X, Li Y, Gu L, Swierczek K, High-performance anode material $Sr_2FeMo_{0.65}Ni_{0.35}O_{6-\delta}$ with in situ exsolved nanoparticle catalyst. *ACS Nano* 2016; 10: 8660-8669. https://doi.org/10.1021/acsnano.6b03979

[19] Zhao D, Zhang K, He T, Yu N, Zhao Y, Wang Y, Liu T, Preparation and characterization of a redox-stable $Pr_{0.4}Sr_{0.6}Fe_{0.875}Mo_{0.125}O_{3-\delta}$ material as a novel symmetrical electrode for solid oxide cell application, *Int J Hydrogen Energy* 2020; 45: 21825-21835. http://dx.doi.org/10.1016/j.ijhydene.2020.05.206

[20] Li Y, Hu B, Xia C, Xu WQ, Lemmon JP, Chen F, A novel fuel electrode enabling direct CO_2 electrolysis with excellent and stable cell performance. *J Mater Chem A* 2017; 5: 20833-20842.

https://doi.org/10.1039/C7TA05750D

[21] Liu T, Zhao Y, Zhang X, Zhang H, Jiang G, Zhao W, Guo J, Chen F, Yan M, Zhang Y, Wang Y, Robust redox-reversible perovskite type steam electrolyser electrode decorated with in situ exsolved metallic nanoparticles, *J Mater Chem A* 2020; 8: 582-591. https://doi.org/10.1039/C9TA06309A

[22] Tao S, Irvine JTS, A redox-stable efficient anode for solid-oxide fuel cells. *Nat Mater* 2003; 2: 320-323. https://doi.org/10.1038/nmat871

[23] Ruiz-Morales JC, Canales-Vázquez J, Peña-Martínez J, López DM, Núñez P, On the simultaneous use of $La_{0.75}Sr_{0.25}Cr_{0.5}Mn_{0.5}O_{3-\delta}$ as both anode and cathode material with improved microstructure in solid oxide fuel cells. *Electrochim Acta* 2006; 52: 278-284. https://doi.org/10.1016/j.electacta.2006.05.006

[24] Cai W, Zhou M, Cao D, Yan X, Li Q, Lü S, Mao C, Li Y, Xie Y, Zhao C, Yu J, Ni M, Liu J, Wang H, Ni-doped A-site-deficient $La_{0.7}Sr_{0.3}Cr_{0.5}Mn_{0.5}O_{3-\delta}$ perovskite as anode of direct carbon solid oxide fuel cells, *Int J Hydrogen Energy* 2020; 45: 21873-21880. https://doi.org/10.1016/j.ijhydene.2020.05.266

[25] Zhou X, Yan N, Chuang KT, Luo J, Progress in La-doped $SrTiO_3$ (LST)-based anode materials for solid oxide fuel cells. *RSC Adv* 2014; 4: 118-131. https://doi.org/10.1039/C3RA42666A

[26] Ruiz-Morales JC, Canales-Vazquez J, Savaniu C, Marrero-Lopez D, Zhou W, Irvine JTS, Disruption of extended defects in solid oxide fuel cell anodes for methane oxidation. *Nature* 2006; 439: 568-571. https://doi.org/10.1038/nature04438

[27] Mizera A, Łącz A, Drożdż E, Synthesis and properties of the materials in $Ni/SrTi_{1-x}Cr_xO_3$ system. *Ceram Int* 2019; 45: 21235-21241. https://doi.org/10.1016/j.ceramint.2019.07.105

[28] Gomez SY, Hotza D, Current developments in reversible solid oxide fuel cells. *Renew Sust Energ Rev* 2016; 61: 155-174. https://doi.org/10.1016/j.rser.2016.03.005

[29] Shu L, Sunarso J, Hashim S S, Mao J, Zhou W, Liang F, Advanced perovskite anodes for solid oxide fuel cells: A review. *Int J Hydrogen Energy* 2019, 44(59): 31275-31304. https://doi.org/10.1016/j.ijhydene.2019.09.220

[30] Dowd Jr R P, Lee S, Fan Y, Gerdes K, Engineering the solid oxide fuel cell electrocatalyst infiltration technique for industrial use. *Int J Hydrogen Energy* 2016, 41(33): 14971-14981. https://doi.org/10.1016/j.ijhydene.2016.06.015

[31] Liu T, Liu H, Zhang X, Lei L, ZhangY, Yuan Z, Chen F, Wang Y, A robust solid oxide electrolyzer for highly efficient electrochemical reforming of methane and steam. *J Mater Chem A* 2019; 7: 13550-13558. https://doi.org/10.1039/C9TA00467J

[32] Wang Y, Xu J, Meng X, Liu T, Chen F, Ni infiltrated $Sr_2Fe_{1.5}Mo_{0.5}O_{6-\delta}$-$Ce_{0.8}Sm_{0.2}O_{1.9}$ electrode for methane assisted steam electrolysis process. *Electrochem Commun* 2017; 79: 63-67. https://doi.org/10.1016/j.elecom.2017.04.018

[33] Rath MK, Lee KT, Superior electrochemical performance of non-precious Co-Ni-Mo alloy catalyst-impregnated $Sr_2FeMoO_{6-\delta}$ as an electrode material for symmetric solid oxide fuel cells. *Electrochim Acta* 2016; 212: 678- 685. https://doi.org/10.1016/j.electacta.2016.07.037

[34] Hua B, Li M, Zhang Y, Chen J, Sun Y, Yan N, Li J, Luo J, Facile synthesis of highly active and robust Ni–Mo bimetallic electrocatalyst for hydrocarbon oxidation in solid oxide fuel cells. *ACS Energy Lett* 2016; 1: 225-230. https://doi.org/10.1021/acsenergylett.6b00109

[35] Ni C, Lu L, Miller DM, Cassidy M, Irvine JTS, Microstructure dependence of performance degradation for intermediate temperature solid oxide fuel cells based on the metallic catalyst

623 infiltrated La-and Ca-doped $SrTiO_3$ anode support. *J Mater Chem A* 2018; 6: 5398-5406.
624 https://doi.org/10.1039/C7TA09534A
625 [36] Thieu CA, Ji H, Kim H, Yoon KJ, Lee JH, Son JW, Palladium incorporation at the anode of thin-
626 film solid oxide fuel cells and its effect on direct utilization of butane fuel at 600 °C. *Appl Energ*
627 2019; 243: 155-164. https://doi.org/10.1016/j.apenergy.2019.03.203
628 [37] Futamura S, Muramoto A, Tachikawa Y, Matsuda J, Lyth SM, Shiratori Y, Taniuchi S, Sasaki K,
629 SOFC anodes impregnated with noble metal catalyst nanoparticles for high fuel utilization. *Int*
630 *J Hydrogen Energy* 2019; 44: 8502-8518.. https://doi.org/10.1016/j.ijhydene.2019.01.223
631 [38] Xu J, Zhou X, Dong X, Pan L, Sun K, Catalytic activity of infiltrated $La_{0.3}Sr_{0.7}Ti_{0.3}Fe_{0.7}O_{3-\delta}$–$CeO_2$
632 as a composite SOFC anode material for H_2 and CO oxidation. *Int J Hydrogen Energy* 2017,
633 42(23): 15632-15640. https://doi.org/10.1016/j.ijhydene.2017.05.016
634 [39] Mehran M T, Khan M Z, Lee S-B, Lim T-H, Park S, Song R-H, Improving sulfur tolerance of Ni-
635 YSZ anodes of solid oxide fuel cells by optimization of microstructure and operating conditions.
636 *Int J Hydrogen Energy* 2018, 43(24): 11202-11213.
637 https://doi.org/10.1016/j.ijhydene.2018.04.200
638 [40] Gasper P J, Lu Y, Nikiforov A Y, Basu S N, Gopalan S, Pal U B, Detailed electrochemical
639 performance and microstructural characterization of nickel-yttria stabilized zirconia cermet
640 anodes infiltrated with nickel, gadolinium doped ceria, and nickel – Gadolinium doped ceria
641 nanoparticles. *J. Power Sources* 2020, 447: 227357.
642 https://doi.org/10.1016/j.jpowsour.2019.227357
643 [41] Xiao P, Ge X, Zhang L, Lee J-M, Wang J-Y, Wang X, H_2 and CH_4 oxidation on $Gd_{0.2}Ce_{0.8}O_{1.9}$
644 infiltrated $SrMoO_3$–yttria-stabilized zirconia anode for solid oxide fuel cells. *Int J Hydrogen*

645 *Energy* 2012, 37(23): 18349-18356. https://doi.org/10.1016/j.ijhydene.2012.08.131

646 [42] Hua B, Li M, Sun Y-F, Zhang Y-Q, Yan N, Li J, Etsell T, Sarkar P, Luo J-L, Grafting doped manganite
647 into nickel anode enables efficient and durable energy conversions in biogas solid oxide fuel
648 cells. *Appl Catal. B-Envrion* 2017, 200: 174-181. https://doi.org/10.1016/j.apcatb.2016.07.001

649 [43] Kwon Y, Kang S, Bae J, Development of a $PrBaMn_2O_{5+\delta}$-$La_{0.8}Sr_{0.2}Ga_{0.85}Mg_{0.15}O_{3-\delta}$ composite
650 electrode by scaffold infiltration for reversible solid oxide fuel cell applications. *Int J Hydrogen*
651 *Energy* 2020, 45(3): 1748-1758. https://doi.org/10.1016/j.ijhydene.2019.11.054

652 [44] Li Y, Zou S, Ju J, Xia C, Characteristics of nano-structured SFM infiltrated onto YSZ backbone for
653 symmetrical and reversible solid oxide cells. *Solid State Ionics* 2018, 319: 98-104.
654 https://doi.org/10.1016/j.ssi.2018.02.003

655 [45] Ding D, Li X, Lai SY, Gerdes K, Liu M, Enhancing SOFC cathode performance by surface
656 modification through infiltration. *Energ Environ Sci* 2014; 7: 552-575.
657 https://doi.org/10.1039/C3EE42926A

658 [46] Connor PA, Yue X, Savaniu CD, Price R, Triantafyllou G, Cassidy M, Kerherve G, Payne DJ, Maher
659 RC, Cohen LF, Tomov RI, Glowacki BA, Kumar RV, Irvine JTS,. Tailoring SOFC electrode
660 microstructures for improved performance. *Adv Energy Mater* 2018; 8: 1800120.
661 https://doi.org/10.1002/aenm.201800120

662 [47] Chrzan A, Karczewski J, Gazda M, Szyczewska D, Jasinski P, $La_{0.6}Sr_{0.4}Co_{0.2}Fe_{0.8}O_{3-\delta}$ oxygen
663 electrodes for solid oxide cells prepared by polymer precursor and nitrates solution infiltration
664 into gadolinium doped ceria backbone, *J Euro Ceram Soc* 2017; 37: 3559-3564.
665 https://doi.org/10.1016/j.jeurceramsoc.2017.04.032

666 [48] Hong T, Zhao M, Brinkman K, Chen F, Xia C, Enhanced oxygen reduction activity on Ruddlesden–

667 Popper phase decorated $La_{0.8}Sr_{0.2}FeO_{3-\delta}$ 3D heterostructured cathode for solid oxide fuel cells.
668 *ACS Appl Mater Interfaces* 2017; 9: 8659-8668. https://doi.org/10.1021/acsami.6b14625
669 [49] Chen Y, Choi YM, Yoo S, Ding Y, Yan RQ, Pei K, Qu C, Zhang L, Chang I, Zhao BT, Zhang YX,
670 Chen HJ, Chen Y, Yang CH, deGlee B, Murphy R, Liu J, Liu ML, A highly efficient multi-phase
671 catalyst dramatically enhances the rate of oxygen reduction. *Joule* 2018; 2: 938-949.
672 https://doi.org/10.1016/j.joule.2018.02.008
673 [50] Ding X, Liu H, Gao Z, Hua G, Wang L, Ding L, Yuan G, $La_{0.6}Ca_{0.4}Fe_{0.8}Ni_{0.2}O_{3-\delta}$ – $Sm_{0.2}Ce_{0.8}O_{1.9}$
674 composites as symmetrical bi-electrodes for solid oxide fuel cells through infiltration and in-
675 situ exsolution. *Int J Hydrogen Energy* 2017; 42(39): 24968-24977.
676 https://doi.org/10.1016/j.ijhydene.2017.08.089
677 [51] Jiang SP, Nanoscale and nano-structured electrodes of solid oxide fuel cells by infiltration: Advances
678 and challenges. *Int J Hydrogen Energy* 2012; 37: 449-470.
679 https://doi.org/10.1016/j.ijhydene.2011.09.067
680 [52] Gong Y, Patel RL, Liang X, Palacio D, Song X, Goodenough JB, Huang K, Atomic layer deposition
681 functionalized composite SOFC cathode $La_{0.6}Sr_{0.4}Fe_{0.8}Co_{0.2}O_{3-\delta}$-$Gd_{0.2}Ce_{0.8}O_{1.9}$ enhanced long-
682 term stability. *Chem Mater* 2013; 25: 4224-4231. https://doi.org/10.1021/cm402879r
683 [53] Ding D, Liu M, Liu Z, Li X, Blinn K, Zhu X, Liu M, Efficient electro-catalysts for enhancing surface
684 activity and stability of SOFC cathodes. *Adv Energy Mater* 2013; 3: 1149-1154.
685 https://doi.org/10.1002/aenm.201200984
686 [54] Li M, Hua B, Zeng Y, Amirkhiz BS, Luo J, Thermally stable and coking resistant CoMo alloy-based
687 catalysts as fuel electrodes for solid oxide electrochemical cells. *J Mater Chem A* 2018; 6:
688 15377-15385. https://doi.org/10.1039/C8TA04749A

689 [55] Adijanto L, Sampath A, Yu AS, Cargnello M, Fornasiero P, Gorte RJ, Vohs JM, Synthesis and
690 stability of Pd@CeO_2 core–shell catalyst films in solid oxide fuel cell anodes. *ACS Catal* 2013;
691 3: 1801-1809. https://doi.org/10.1021/cs4004112
692 [56] Lv H, Zhou Y, Zhang X, Song Y, Liu Q, Wang G, Bao X, Infiltration of $Ce_{0.8}Gd_{0.2}O_{1.9}$ nanoparticles
693 on $Sr_2Fe_{1.5}Mo_{0.5}O_{6-\delta}$ cathode for CO_2 electroreduction in solid oxide electrolysis cell. *J Energy*
694 *Chem* 2019; 35: 71-78. https://doi.org/10.1016/j.jechem.2018.11.002
695 [57] Liu T, Zhao Y, Zhang X, Zhang H, Jiang G, Zhao W, Guo J, Chen F, Yan M, Zhang Y, Wang Y,
696 Robust redox-reversible perovskite type steam electrolyser electrode decorated with in situ
697 exsolved metallic nanoparticles. *J Mater Chem A* 2020; 2: 582-591.
698 https://doi.org/10.1039/C9TA06309A
699 [58] Zhang T, Zhao Y, Zhang X, Zhang H, Yu N, Liu T, Wang Y, Thermal stability of an in situ exsolved
700 metallic nanoparticle structured perovskite type hydrogen electrode for solid oxide cells. *ACS*
701 *Sustain Chem Eng* 2019; 7: 17834-17844. https://doi.org/10.1021/acssuschemeng.9b04350
702 [59] Wan S, Yan M, Zhang Y, A numerical study of infiltrated solid oxide fuel cell electrode with dual-
703 phase backbone. *Int J Energ Res* 2019; 43: 2562-2570. https://doi.org/10.1002/er.4129
704 [60] Zhang Y, Yan M, Wan Y, Jiao Z, Chen Y, Chen F, Xia C, Ni M, High-throughput 3D reconstruction
705 of stochastic heterogeneous microstructures in energy storage materials. *npj Comput Mater*
706 2019; 5: 11. https://doi.org/10.1038/s41524-019-0149-4
707 [61] Dong J, Cheng Z, Zha SW, Liu ML, Identification of nickel sulfides on Ni–YSZ cermet exposed to
708 H_2 fuel containing H_2S using Raman spectroscopy. *J Power Sources* 2006; 156: 461-465.
709 https://doi.org/10.1016/j.jpowsour.2005.06.016
710 [62] Harboe S, Lupetin P, Guillon O, Menzler NH, Investigation of LSM/8YSZ cathode within an all-

ceramic SOFC, Part II: Optimization of performance and co-sinterability, *J Euro Ceram Soc* 2020; 40: 3618-3631. https://doi.org/10.1016/j.jeurceramsoc.2020.03.010

[63] Gopal C B, Haile S M, An electrical conductivity relaxation study of oxygen transport in samarium doped ceria. *J Mater Chem A* 2014, 2(7): 2405-2417. https://doi.org/10.1039/C3TA13404K

[64] Wang Y, Hu B, Zhu Z, Bouwmeester HJM, Xia C, Electrical conductivity relaxation of $Sr_2Fe_{1.5}Mo_{0.5}O_{6-\delta}$–$Sm_{0.2}Ce_{0.8}O_{1.9}$ dual-phase composites. *J Mater Chem A* 2014; 2: 136-143. https://doi.org/10.1039/C3TA12787G

[65] Hu B, Wang Y, Zhu Z, Xia C, Bouwmeester HJM, Measuring oxygen surface exchange kinetics on mixed-conducting composites by electrical conductivity relaxation. *J Mater Chem A* 2015; 3: 10296-10302. https://doi.org/10.1039/C5TA00510H

[66] Li L, Kong Z, Yao B, Yang H, Gao Z, Xu L, Dong F, Ni M, Lin Z, An efficient and durable perovskite electrocatalyst for oxygen reduction in solid oxide fuel cells, *Chem Eng J* 2020; 396: 125237. https://doi.org/10.1016/j.cej.2020.125237

[67] Zhang Y, Sun Q, Xia C, Ni M, Geometric properties of nanostructured solid oxide fuel cell electrodes. *J Electrochem Soc* 2013; 160: F278-F289. https://doi.org/10.1149/2.057303jes